

# Closed-Loop Magnetic Control of Medical Soft Continuum Robots for Deflection

Zhiwei Wu<sup>id</sup>, Graduate Student Member, Jinhui Zhang<sup>id</sup>

**Abstract**—Magnetic soft continuum robots (MSCRs) have emerged as powerful devices in endovascular interventions owing to their hyperelastic fibre matrix and enhanced magnetic manipulability. Effective closed-loop control of tethered magnetic devices contributes to the achievement of autonomous vascular robotic surgery. In this article, we employ a magnetic actuation system equipped with a single rotatable permanent magnet to achieve closed-loop deflection control of the MSCR. To this end, we establish a differential kinematic model of MSCRs exposed to non-uniform magnetic fields. The relationship between the existence and uniqueness of Jacobian and the geometric position between robots is deduced. The control direction induced by Jacobian is demonstrated to be crucial in simulations. Then, the corresponding quasi-static control (QSC) framework integrates a linear extended state observer to estimate model uncertainties. Finally, the effectiveness of the proposed QSC framework is validated through comparative trajectory tracking experiments with the PD controller under external disturbances. Further extensions are made for the Jacobian to path-following control at the distal end position. The proposed control framework prevents the actuator from reaching the joint limit and achieves fast and low error-tracking performance without overshooting.

**Index Terms**—Magnetic soft continuum robots, permanent magnet, closed-loop deflection control, quasi-static controller

## I. INTRODUCTION

MAGNETICALLY-ACTUATED robotic-assisted surgery has garnered considerable attention and found extensive applications in vascular interventions recently. A well-established magnetic-actuated surgical robotic system typically consists of a designable and programmable magnetic field generator, a magnetic continuum robot capable of precise manipulation within the patient’s vasculature using the generated field, and various complementary devices. In comparison to conventional robot-assisted interventions, the magnetic field demonstrates remarkable and secure penetration through human tissues, facilitating contactless object manipulation [1]. The inherent compliance and flexibility of the magnetic continuum robot enable predictable deflection without applying torsion, thereby allowing convenient navigation through intricate and narrow vasculatures, including bifurcations.

Systems equipped with electromagnets have been developed as laboratorial and commercial products for remote navigation of magnetic devices [2]–[4]. The systems are designed to precisely manipulate the directionality of the generated magnetic field, simplifying the control challenges associated with magnetic devices. However, the structural openness of the

electromagnetic systems restricts the size of the workspace, and the resulting thermal effects may pose potential safety risks to the human body [5]. In contrast, permanent magnets serve as ideal actuating devices in clinical settings, providing stable and powerful magnetic fields. Cutting-edge commercial systems incorporate a pair of large permanent magnets symmetrically positioned on either side of the patient [6], obtaining FDA certification and demonstrating significant success in cardiac ablation procedures [7]. However, the expensive price, considerable volume, and challenges in downsizing the equipment pose obstacles to its deployment in primary healthcare facilities. Alternatively, the single permanent magnet offers affordability and compact size, allowing for convenient attachment with robot arms and enabling remote manipulation [8]. This compact actuating system, initially used in endoscopy departments, has been recognized for its feasibility in neurovascular interventions [9]. The achievement is mostly attributed to the development of novel magnetic soft continuum robots (MSCRs) fabricated using hard-magnetic soft composites [10]. MSCRs evade the intravascular detachment of micromagnets in commercially available magnetic devices while also providing enhanced slimness and flexibility beyond the magnet thickness limit.

In advancing towards high-level/full autonomy, closed-loop control of tethered magnetic devices is a critical component in endovascular robotic surgery [11]. It effectively mitigates the complex nonlinear behaviour of continuum robots and assists clinical practitioners in shifting their focus from operational tasks to more intricate medical procedures. The electromagnetic system has emerged as the initial choice for implementing closed-loop control due to its capability of generating simple and uniform magnetic fields [12], [13]. Although attempts have been made to incorporate permanent magnet systems with multi-actuate-magnets [14], the prevalent approach still relies on open-loop control schemes [15]–[18], possibly because of the complex geometric shape of the dipole field generated by permanent magnets. Therefore, the aim of this paper is to establish a differential kinematic model for magnetic soft composite material robots in non-uniform gradient magnetic fields and propose an observer-integrated quasi-static controller to achieve closed-loop deflection control with only a single actuating magnet. The main contributions can be summarized into the following threefolds:

- 1) The three-dimensional kinematic model is established for the MSCR under a magnetic dipole field. Theorems to determine the minimum distance between the robot and the magnet are proposed, ensuring the existence

Z. Wu, J. Zhang are with the School of Automation, Beijing Institute of Technology, Beijing, 100081, China (e-mail: 3120220885@bit.edu.cn; zhangjinh@bit.edu.cn). (Corresponding author: Jinhui Zhang, phone: +86 10 68914350; fax: +86 10 68914382).

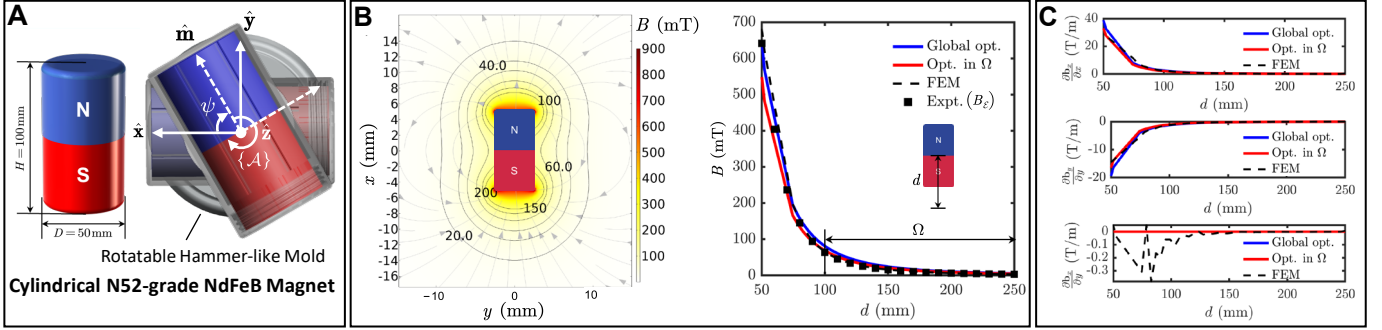


Fig. 1. Small rotatable magnetic equipment. (A) Cylindrical N52-grade NdFeB magnet loaded in a rotatable hammer-like mold. (B) (left) Axis-symmetric magnetic field distribution around the magnet with remanence  $B_{re} = 1.44$  T. (right) Comparison of the analytical solutions of the magnetic flux density  $\|\mathbf{b}\|$  (noted in B) along the principle axis at distance  $d$  with the finite element method (FEM) and experiments. (C) Comparison of the spatial gradient magnetic field along the principle axis of the magnet in the distance  $d$  between analytical solutions and FEM results ( $\hat{\mathbf{x}}_A$ - $\hat{\mathbf{y}}_A$  plane).

and uniqueness of the Jacobian. The model accuracy is verified by comparing the singularities with experimental measurements.

- 2) The controllability of the differential kinematic model for MSCR is proved. Based on this model, a quasi-static controller (QSC) for closed-loop deflection control is designed, incorporating a linear extended state observer to compensate for model uncertainties and disturbances.
- 3) A visual detection algorithm for tracking the tip deflection angle of MSCR is deployed. The control performance of QSC is compared with that of a PD controller under various tracking signals and external disturbances. The Jacobian-based to distal end positional control is further explored.

The remainder of this paper is organized as follows: Section II studies the mathematical model of the permanent magnet and MSCR. Section III discusses the Jacobian singularity and proposes the quasi-static controller. Simulations and experiments are conducted in Section IV. Section V explores the position control of the MCSR, and VI concludes this paper.

## II. MATHEMATICAL MODELING

Throughout the technical note, vectors are denoted in lower case, bold font (e.g.  $\mathbf{x}$ ), and with an extra ‘hat’ symbol to be unit (e.g.  $\hat{\mathbf{x}}$ ). Scalars are denoted by Italy font (e.g.  $X$ ), and matrices are denoted by Roman font (e.g.  $X$ ).  $\|\cdot\|$  denotes the  $\mathcal{L}_2$  norm for any tensor. The identity matrix is denoted by  $\mathbb{I}$  with a subscript indicating the appropriate dimensions.

### A. Small Rotatable Magnetic Equipment

Permanent magnets, serving as effective drivers for magnetic devices, are capable of generating non-uniform gradient magnetic fields. Embedding magnets within a designed hammer-shaped mold to attach to a robotic arm allows for the manipulation of magnetic devices by altering the spatial positioning and orientation of the magnet. The end-effector mechanism, referred to as the small rotatable magnetic equipment (RME), contains an axially magnetized cylindrical N52-grade NdFeB magnet with diameter  $D = 50$  mm, height  $H = 100$  mm, and remanence  $B_{re} = 1.44$  T. The magnet is loaded in a rotatable hammer-like mold with an attached

frame  $\{A\}$  positioned at the geometric center  $\mathbf{p}_A \in \mathbb{R}^3$ , where the  $\hat{\mathbf{x}}_A$ -axis initially coincides with the dipole moment  $\mathbf{m}_A \in \mathbb{R}^3$  (the vector from south to north pole). As shown in Fig. 1.A, the magnet can rotate along the  $\hat{\mathbf{z}}_A$ -axis that is perpendicular to the principal axis. The rotation angle  $\psi$  is defined to be clockwise positive, yielding the relations between  $\psi$  and  $\hat{\mathbf{m}}_A$  as  $\hat{\mathbf{m}}_A = [\cos \psi, \sin \psi, 0]^\top$ . The magnetic field  $\mathbf{b}(\mathbf{p}, \hat{\mathbf{m}}_A) \in \mathbb{R}^3$  generated by the cylindrical magnet in any spatial point  $\mathbf{p}_S \in \mathbb{R}^3$  is assumed to be modeled by the point dipole model [19], which is provided by

$$\mathbf{b}(\mathbf{p}, \hat{\mathbf{m}}_A) = \frac{\mu_0 M_A}{4\pi \|\mathbf{p}\|^3} (3\hat{\mathbf{p}}\hat{\mathbf{p}}^\top - \mathbb{I}_3) \hat{\mathbf{m}}_A, \quad (1)$$

where  $\mathbf{p} = \mathbf{p}_S - \mathbf{p}_A$ ,  $\mu_0$  denotes the space permeability, and  $M_A = \|\mathbf{m}_A\|$  is the dipole moment modulus to be estimated. The magnetic field distribution is simulated using the finite-element method (FEM) via COMSOL v5.6 and demonstrated in Fig. 1.B (left). The field directions, indicated by gray lines with arrows, show that the S pole of the magnet performs attraction to magnetic devices while the N pole performs repulsion. Manipulation distance from  $\mathbf{p}_A$  to magnetic devices is limited to  $\Omega = [100, 250]$  (mm) for surgical safety concerns. Experimental results of the magnetic field modulus  $B$  in the distance  $d$  along the principal axis of the magnet are plotted against the FEM results in Fig. 1.B (right). The magnetic dipole moment modulus  $M_A$  is estimated for global and within the working distance  $\Omega$  optimally using the least square fitting (LSF) as

$$M_A^* = \arg \min_{M_A} \left( \sum_{d \in \Omega} (B_{\mathcal{E}}(d) - B(d, M_A))^2 \right), \quad (2)$$

where  $B_{\mathcal{E}}$  represents experimental results and  $B(d, M_A)$  is the scalar function of  $d$  and  $M_A$ , deduced from (1). As a result, the red line with a reported value of  $M_A^* = 342.86$  A  $\cdot$  m<sup>2</sup> corresponds more closely to the FEM and experimental results within  $\Omega$  than the globally optimal estimated.

The spatial gradient magnetic field  $\nabla \mathbf{b} \in \mathbb{R}^{3 \times 3}$  generated by the cylindrical magnet also contributes to actuate magnetic devices [10]. The expression of  $\nabla \mathbf{b}$  is derived from (1) as

$$\nabla \mathbf{b} = \frac{3\mu_0 M_A}{4\pi \|\mathbf{p}\|^4} (\hat{\mathbf{p}}\hat{\mathbf{m}}_A^\top + \hat{\mathbf{p}}^\top \hat{\mathbf{m}}_A \mathbb{I}_3 + \mathbf{Z}\hat{\mathbf{m}}_A \hat{\mathbf{p}}^\top), \quad (3)$$

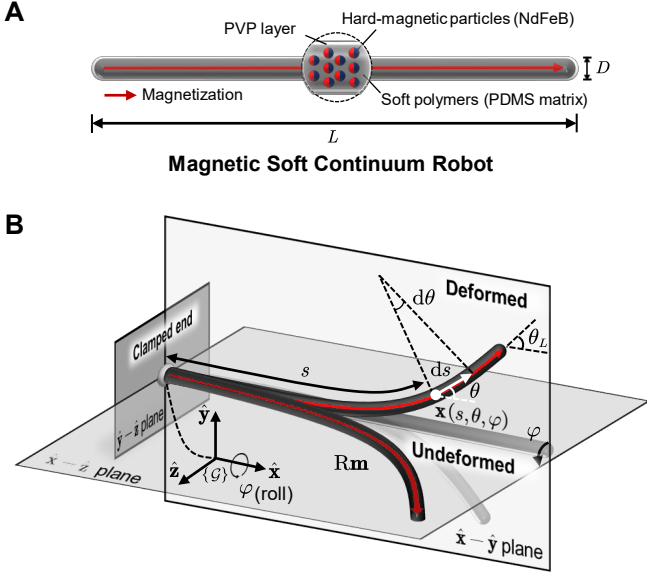


Fig. 2. Magnetic soft continuum robot (MSCR). (A) The material composition of the axially magnetized MSCR of length  $L$  and diameter  $D$ . (B) A kinematic schematic of the MSCR in configuration space of  $(s, \theta, \varphi)$ .

where  $Z = \mathbb{I}_3 - 5\hat{\mathbf{p}}\hat{\mathbf{p}}^\top$ . Appropriate quasi-static simplifications of Maxwell's equations ( $\nabla \cdot \mathbf{b} = 0$ ) and no current flow assumption ( $\nabla \times \mathbf{b} = 0$ ) in robotic applications limit the number of truly independent quantities in gradient magnetic field [20]. The symmetry property is also reflected in (3) so that  $\frac{\partial \mathbf{b}_x}{\partial y} = \frac{\partial \mathbf{b}_y}{\partial x} = 0$ . It can be observed in Fig. 1.C that the red line presents good predictions for all three independent quantities of the gradient magnetic field along the principle axis in the distance  $d$  within  $\Omega$ . However, the blue line with globally optimal estimated  $M_A$  appears to be more aggressive when compared with the FEM results. The reason might be that the point-dipole model takes no consideration of the magnet's geometric shape and an incomplete simplified resolution of the magnetic field is being used.

### B. Magnetic Soft Continuum Robot

The slender magnetic soft continuum robot, whose diameter  $D$  is much less than its length  $L$ , is fabricated by injection molding with hard-magnetic soft composites where the fillers comprise soft polymers (PDMS matrix) and hard-magnetic particles (6.5- $\mu\text{m}$ -sized NdFeB). As shown in Fig. 2.A, the lateral surface of the MSCR is encased by polyvinylpyrrolidone (PVP) thin layer, providing biocompatible, noncytotoxic, and hydrophilic properties in contact with vasculatures. Moreover, magnetic moments of the internal microparticles are rearranged axially under strong external magnetic fields, resulting in the isotropic and natural straight MSCR being magnetic manipulability in addition to super-elasticity.

The MSCR is modeled based on the hard-magnetic elastica theory [21], which parameterized it by a spatial curve  $\theta = \theta(s)$  with an attached frame  $\{\mathcal{G}\}$  at the clamped-proximal end. A schematic of the MSCR is demonstrated in Fig. 2.B. The arc length parameter  $s$  and the tangential angle  $\theta$  uniquely determine the spatial material point  $\mathbf{x}(s, \theta)$  in planar deformed

elastica. Furthermore, with the premise that torsion motion is negligible, the MSCR is capable of rolling along the  $\hat{\mathbf{x}}_G$ -axis. Magnetic steering of the MSCR in planes with specific roll angles (noted as  $\varphi$ -plane) imposes constraints on the origin and orientation of the magnetic field generator, which will be discussed later. As a result, the configuration space of the MSCR is represented by  $(s, \theta, \varphi)$ , and the total Helmholtz free energy density consists of the following two parts:

$$\begin{cases} \Psi^{\text{elastic}}(\theta') = \frac{EI}{2A}\theta'^2 \\ \Psi^{\text{magnetic}}(s, \theta; \varphi) = -\mathbf{Rm} \cdot \mathbf{b}, \end{cases} \quad (4)$$

where  $E, I, A$  represent Young's modulus, the second moment of inertia, and the cross-sectional area of the MSCR, respectively. The curvature  $\kappa(s) = \frac{d\theta(s)}{ds} = \theta'(s)$  forms a quadratic expression  $\Psi^{\text{elastic}}(\theta')$  of the elastic part. In respect to the magnetic part, the axial magnetization vector  $\mathbf{m} \in \mathbb{R}^3$ , referred to the undeformed state, is premultiplied by a rotation matrix  $\mathbf{R}(\varphi, \theta) \in SO(3)$  in the  $\varphi$ -plane as  $\mathbf{R}(\varphi, \theta)\mathbf{m} = \text{Rot}(\hat{\mathbf{x}}_G, \varphi)\text{Rot}(\hat{\mathbf{z}}_G, \theta)\mathbf{m}$ , where  $\text{Rot}(\cdot, \cdot)$  is known as Rodrigues' formula for rotations. The external magnetic field  $\mathbf{b}(\mathbf{p}, \hat{\mathbf{m}}_A)$  is generated by the cylindrical magnet, in which  $\mathbf{p}_S$  is replaced by the material point  $\mathbf{x}$  of interest. The total Helmholtz free energy density as a function of four variables  $(s, \theta, \theta'; \varphi) : \Psi(s, \theta, \theta'; \varphi) = \Psi^{\text{elastic}}(\theta') + \Psi^{\text{magnetic}}(s, \theta; \varphi)$ . Then, the equilibrium state in arbitrary  $\varphi$ -planes can be described by the Euler-Lagrange equation:  $\frac{d}{ds} \left( \frac{\partial \Psi}{\partial \theta'} \right) = \frac{\partial \Psi}{\partial \theta}$ , from which yields the kinematics, or the governing equation, of the MSCR as

$$\frac{EI}{A} \frac{d^2\theta}{ds^2} = -\frac{\partial}{\partial \theta} (\mathbf{Rm} \cdot \mathbf{b}). \quad (5)$$

With the help of the chain rule, the right-hand side can be expanded as  $\frac{\partial}{\partial \theta} (\mathbf{Rm} \cdot \mathbf{b}) = \frac{\partial \mathbf{R}}{\partial \theta} \mathbf{m} \cdot \mathbf{b} + [(\nabla \mathbf{b})^\top \mathbf{Rm}] \cdot \frac{\partial \mathbf{x}}{\partial \theta}$ , where the material point  $\mathbf{x}$  on the MSCR satisfies the following kinematic relations:

$$\mathbf{x} = \text{Rot}(\hat{\mathbf{x}}_G, \varphi) \left[ \int_0^s \cos \theta(\eta) d\eta \hat{\mathbf{x}}_G + \int_0^s \sin \theta(\eta) d\eta \hat{\mathbf{y}}_G \right]$$

and

$$\frac{\partial \mathbf{x}}{\partial \theta} = \text{Rot}(\hat{\mathbf{x}}_G, \varphi) \left[ -\int_0^s \sin \theta(\eta) d\eta \hat{\mathbf{x}}_G + \int_0^s \cos \theta(\eta) d\eta \hat{\mathbf{y}}_G \right].$$

To study the response of the MSCR's distal end under non-uniform magnetic fields, the governing equation (5) is written in the canonical form with boundary conditions as

$$\frac{d^2\theta}{ds^2} = \sigma(s, \theta; \varphi). \quad \text{s.t.} \quad \theta(0) = 0, \quad \theta'(L) = 0, \quad (6)$$

which is referred to as the two-point boundary-value problem (BVP). The crucial assumption that assists in establishing the existence of the solution  $\theta(s)$  is presented as follows.

**Assumption 1.** The position of the permanent magnet  $\mathbf{p}_A$  satisfies  $\|\mathbf{p}_A - \mathbf{x}(s)\| > 0, \forall s \in [0, L]$ .

**Theorem 1.** The governing equation (6) for the MSCR has solutions  $\theta(s)$  if the Assumption 1 is satisfied.

**Remark 1.** Let  $\|\mathbf{p}_A - \mathbf{x}(s)\| \geq \|\mathbf{p}_A\| - L > 0$ , this strong condition provides a feasibility scenario for Assumption 1 to



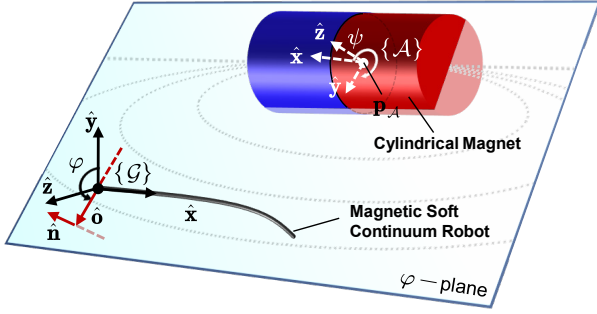


Fig. 3. A feasible scheme for deflecting the MSCR in a specific plane. The geometry of the  $\varphi$ -plane is characterized by the normal  $\hat{\mathbf{n}}$  and the unit vector of intersection line  $\hat{\mathbf{o}}$  in frame  $\{\mathcal{G}\}$ . The cylindrical magnet with desired configuration  $\mathbf{T}_{\mathcal{G}\mathcal{A}}^d$  is located in the  $\varphi$ -plane and the rotation axis  $\hat{\mathbf{z}}_{\mathcal{A}}$  coincides with  $\hat{\mathbf{n}}$ .

hold. For practical implementations, the physical collision between the magnet and the MSCR requires consideration. One measure that can be taken is to ensure that the manipulation distance falls within the  $\Omega$  interval designed in Section II-A.

**Remark 2.** Some sufficient condition results on proofs of uniqueness have been made in the literature [22], indicating that the solution  $\theta(s)$  is unique when  $\frac{\partial\sigma(s,\theta)}{\partial\theta} > 0$  in certain regions.

The proof of Theorem 1 is postponed to be completed in the Appendix.A for readability. The solution to this problem will require the use of numerical methods, such as the shooting method or collocation. Let  $\theta_L = \theta(L)$  be the rotation angle of the distal end, the integral equation of (6) reads

$$\theta_L = \int_0^L \int_0^\zeta \sigma(s, \theta; \varphi) ds d\zeta = \vartheta(\mathbf{p}_{\mathcal{G}}, \psi), \quad (7)$$

where  $\vartheta: \mathbb{R}^3 \times \mathbb{R} \rightarrow \Theta$  represents the map from the control inputs to the workspace  $\Theta$  of the MSCR. Recall that the configuration space (C-space) of the MSCR is represented by  $(s, \theta, \varphi)$ , of which the premise is that the robot always performs planar deflection. As illustrated in Fig. 3, a feasible scheme is to constrain the origin of the magnetic field generator  $\mathbf{p}_{\mathcal{A}}$  located in the  $\varphi$ -plane and to rotate only about the normal  $\hat{\mathbf{n}}$ . Specifically, the unit vector of intersection line  $\hat{\mathbf{o}}$  and the normal  $\hat{\mathbf{n}}$  of the  $\varphi$ -plane are present in frame  $\{\mathcal{G}\}$  as  $\hat{\mathbf{o}}_{\mathcal{G}} = [0, \cos \varphi, \sin \varphi]^\top$  and  $\hat{\mathbf{n}}_{\mathcal{G}} = [0, \sin \varphi, -\cos \varphi]^\top$ . Then, the desired configuration of the cylindrical magnet is represented in frame  $\{\mathcal{G}\}$  by the homogeneous matrix  $\mathbf{T}_{\mathcal{G}\mathcal{A}}^d = (\text{Rot}(\hat{\mathbf{n}}_{\mathcal{G}}, \psi) \mathbf{R}_{\mathcal{G}\mathcal{A}}^d(\varphi), \mathbf{p}_{\mathcal{G}\mathcal{A}}^d) \in SE(3)$ , where  $\mathbf{R}_{\mathcal{G}\mathcal{A}}^d(\varphi) = [-\hat{\mathbf{x}}_{\mathcal{G}}, \hat{\mathbf{o}}_{\mathcal{G}}(\varphi), \hat{\mathbf{n}}_{\mathcal{G}}(\varphi)]$  constrains the orientation of the magnet, and  $\mathbf{p}_{\mathcal{G}\mathcal{A}}^d$  satisfies  $\mathbf{p}_{\mathcal{G}\mathcal{A}}^d \cdot \hat{\mathbf{n}} = 0$  to constraint the origin located in the  $\varphi$ -plane. The orientation matrix is premultiplied by  $\text{Rot}(\hat{\mathbf{n}}_{\mathcal{G}}, \psi)$ , indicating the self-rotation of the magnet. In this manner, the principle axis of the rotating magnet stays in the plane with the deformed MSCR body, and, the distal end of the MSCR points to the S pole along symmetrical magnetic field streamlines. Moreover, if the origin  $\mathbf{p}_{\mathcal{A}}$  is fixed, which means that the deformation of the MSCR is dominated by the rotation of the magnet, we are able to represent the C-space using only two variables  $(\theta_L, \varphi)$ .

**Remark 3** (On the C-space Representation). *Soft continuum robots are typically redundant and have theoretically infinite degrees of freedom (DOF). Because the control inputs are also redundant, independently moving or rotating the magnet can deflect the MSCR, making the map  $\vartheta$  surjective to the inputs  $\mathbf{p}_{\mathcal{G}}$  and  $\psi$ . Among all actuated configurations, those with the same  $\theta_L$  but different deformed shapes constitute the null space  $\mathcal{N}(\theta)$  for the tangential angle  $\theta$ . However, as pointed out in Theorem 3, the map  $\psi \mapsto \vartheta(\cdot, \psi)$  is bijective when  $\psi \in \Psi$ , where the null space vanishes. Thus, the deformed MSCR actuated by rotating the magnet has a unique corresponding joint angle.*

### III. QUASI-STATIC CONTROL FRAMEWORK

This section provides a quasi-static control framework for moving the MSCR's equilibrium states from one to another. The input-affine control system of the MSCR based on differential kinematics with analyzed Jacobian perturbation is primarily derived. Then, the linear extended state observer is employed to estimate the perturbation and provide robust control performance.

#### A. Differential Kinematics

To obtain the differential kinematic relation between the control inputs and the rotation angle of the distal end, the magnetic field (1) is re-represented as

$$\mathbf{b} = \bar{\mathbf{B}}(\mathbf{p}_{\mathcal{A}}) \hat{\mathbf{m}}_{\mathcal{A}}(\psi). \quad (8)$$

Note that the control inputs  $\mathbf{p}_{\mathcal{A}}$  and  $\psi$  are separated into a pair of product terms, the same rearrangement can be employed on the gradient magnetic field (3) by introducing an arbitrary vector  $\mathbf{v} \in \mathbb{R}^3$ , yielding the expression:

$$\begin{aligned} (\nabla \mathbf{b})^\top \mathbf{v} &= \frac{3\mu_0 M_{\mathcal{A}}}{4\pi \|\mathbf{p}\|^4} (\hat{\mathbf{p}} \hat{\mathbf{m}}_{\mathcal{A}}^\top + \hat{\mathbf{p}}^\top \hat{\mathbf{m}}_{\mathcal{A}} \mathbb{I}_3 + \mathbf{Z} \hat{\mathbf{m}}_{\mathcal{A}} \hat{\mathbf{p}}^\top) \mathbf{v} \\ &= \frac{3\mu_0 M_{\mathcal{A}}}{4\pi \|\mathbf{p}\|^4} (\hat{\mathbf{p}} \mathbf{v}^\top + \mathbf{v} \hat{\mathbf{p}}^\top + \hat{\mathbf{p}}^\top \mathbf{v} \mathbf{Z}) \hat{\mathbf{m}}_{\mathcal{A}} \\ &= \bar{\mathbf{B}}_g(\mathbf{p}_{\mathcal{A}}, \mathbf{v}) \hat{\mathbf{m}}_{\mathcal{A}}(\psi). \end{aligned} \quad (9)$$

Taking the derivative of  $\theta(s, \theta; \psi)$  with respect to  $\psi$  on (6) yields the Sturm-Liouville boundary-value problem (SL-BVP) that can be solved for the Jacobian  $J(s) \in \mathbb{R}$  along the arc length:

$$\begin{aligned} \frac{d^2 J(s)}{ds^2} &= \frac{\partial \sigma(s, \theta)}{\partial \theta} J(s) + \frac{\partial \sigma(s, \theta; \psi)}{\partial \psi}, \\ \text{s.t. } J(0) &= 0, J'(L) = 0. \end{aligned} \quad (10)$$

To establish the existence and uniqueness of the solution to Jacobian  $J(s)$ , one can make the following assumption that ensures the Lipschitz constant  $K$  derived in the proof of Theorem 1 is satisfied.

**Assumption 2.** *The Lipschitz constant  $K$  satisfies  $K \in \mathcal{K} \triangleq [0, \frac{\pi^2}{4L^2}] \cup [(\frac{-\pi+4k\pi}{2L})^2, (\frac{\pi+4k\pi}{2L})^2]$ ,  $k \in \mathbb{N}$ .*

**Theorem 2.** *SL-BVP (10) has solutions  $J(s)$  if Assumption 1 holds and it is unique when Assumption 2 holds.*

**Remark 4.** Limiting the magnitude of the magnetic field  $B$  enables the Assumption 2 to hold. For  $k = 0$ , the Lipschitz constant is subject to  $0 < K < \left(\frac{\pi}{2L}\right)^2$ . The following numerical simulation results in Section III-B permit us to disregard the norms of higher-order gradient tensors of  $\mathbf{b}$ , leading to an estimated upper bound as  $B < \frac{EI\pi^2}{4MAL^2}$ , which coincides with the critical field strength for MSCR buckling instability given in [23].

For the sake of readability, the proof of Theorem 2 is located in Appendix B. The infinite-dimensional distributed parameter system (DPS) formed by the Jacobian  $J(s)$  provides a control model for any point on the MSCR body. However, in practical applications such as vascular interventions, the tip position and angle of MSCR are of greater concern. Controlling the isolated point ( $s = L$ ) of the DPS system simplifies it into an input-affine nonlinear system. Without loss of generality, consider the scenario of  $\varphi = 0$ , the corresponding rotation matrix reads  $R_{\mathcal{G}\mathcal{A}}(\varphi) = [-\hat{\mathbf{x}}_{\mathcal{G}}, \hat{\mathbf{y}}_{\mathcal{G}}, -\hat{\mathbf{z}}_{\mathcal{G}}]$ , and the unit dipole moment is given by  $\hat{\mathbf{m}}_{\mathcal{G}}(\psi) = R_{\mathcal{G}\mathcal{A}}(\varphi)\hat{\mathbf{m}}_{\mathcal{A}}(\psi) = [-\cos\psi, \sin\psi, 0]^\top$ . Substituting the rearranged expressions (8) and (9) into (7) derives the inputs separated equation that  $\vartheta(\mathbf{p}_{\mathcal{G}}, \psi) = \bar{\vartheta}(\theta; \mathbf{p}_{\mathcal{G}})\hat{\mathbf{m}}_{\mathcal{G}}(\psi)$ , where the details of  $\vartheta(\mathbf{p}_{\mathcal{G}}, \psi)$  are listed in (11). If the origin of the magnet is fixed,  $\bar{\vartheta}(\theta; \mathbf{p}_{\mathcal{G}})$  can be pre-computed. Consequently,  $\hat{\mathbf{m}}_{\mathcal{G}}$  is sorted out that facilitates deriving the partial derivative of  $\theta_L$  with respect to  $\psi$ , which is

$$\begin{aligned} \frac{\partial\theta_L}{\partial\psi} &= \frac{\partial\bar{\vartheta}(\theta; \mathbf{p}_{\mathcal{G}})}{\partial\theta} \frac{\partial\theta}{\partial\psi} \hat{\mathbf{m}}_{\mathcal{G}}(\psi) + \bar{\vartheta}(\theta; \mathbf{p}_{\mathcal{G}}) \frac{\partial\hat{\mathbf{m}}_{\mathcal{G}}(\psi)}{\partial\psi} \\ &= J(s)|_{s=L} \triangleq J_\psi(\mathbf{p}_{\mathcal{G}}, \psi), \end{aligned} \quad (12)$$

where  $J_\psi \in \mathbb{R}$  is the Jacobian of our interested, and  $\frac{\partial\hat{\mathbf{m}}_{\mathcal{G}}(\psi)}{\partial\psi} = [\sin\psi, \cos\psi, 0]^\top$ . Additionally, the partial derivative of  $\theta_L$  with respect to  $\mathbf{p}_{\mathcal{G}}$  is also considered for future reference. With the help of the expression:  $\delta\mathbf{p} = \delta\mathbf{x} - \delta\mathbf{p}_{\mathcal{G}}$ , it can be deduced that  $\frac{\partial\theta_L}{\partial\mathbf{p}_{\mathcal{G}}} = -\frac{\partial\bar{\vartheta}(\theta; \mathbf{p}_{\mathcal{G}})}{\partial\mathbf{p}} \hat{\mathbf{m}}_{\mathcal{G}}(\psi) = J_{\mathbf{p}}(\mathbf{p}_{\mathcal{G}}, \psi)$ , in which  $\frac{\partial\bar{\vartheta}}{\partial\mathbf{p}}$  is a third-order tensor and  $J_{\mathbf{p}} \in \mathbb{R}^{1 \times 3}$ . These results lead us to the differential kinematic equation:

$$\dot{\theta}_L = J_\psi \dot{\psi} + J_{\mathbf{p}} \dot{\mathbf{p}}_{\mathcal{G}}. \quad (13)$$

### B. Analysis of the Jacobian

The analysis of the Jacobian  $J_\psi(\mathbf{p}_{\mathcal{G}}, \psi)$  is discussed in the special case of  $\varphi = 0$ . Notably, this particular scenario holds for  $\varphi \in [0, 2\pi]$ . A preliminary qualitative analysis is conducted on the distal rotation angle  $\theta_L$  of the MSCR, which is obtained from the product of  $\bar{\vartheta}(\mathbf{p}_{\mathcal{G}})$  and  $\hat{\mathbf{m}}_{\mathcal{G}}(\psi)$ . The elements of  $\bar{\vartheta}(\theta; \mathbf{p}_{\mathcal{G}})$  are represented as  $[\vartheta_1, \vartheta_2, *]$ . Subsequently, the expression of  $\theta_L$  can be rewritten using the auxiliary angle formula as

$$\theta_L = -\bar{\vartheta}_1 \cos\psi + \bar{\vartheta}_2 \sin\psi = \bar{\vartheta} \sin(\psi - \psi_0), \quad (14)$$

---

**Algorithm 1:** Computation of deflection angle  $\theta(s)$  and analytical Jacobian  $J(s)$  of the MSCR

---

**Input:** Position  $\mathbf{p}_{\mathcal{G}}$  and rotation angle  $\psi$  of the magnet  
**Output:** Deflection angle  $\theta(s)$  and analytical Jacobian  $J(s)$

- 1 Compute  $\theta(s)$  by solving the BVP (6) using the shooting method [24];
- 2 Compute the initial value problems  $LJ^{(1)}$  and  $LJ^{(2)}$  with the higher order term  $\nabla^2\mathbf{b}$  ignored using numerical integration methods;
- 3 **if** Assumption 2 is satisfied **then**
- 4 | Linear combination factor  $v = -J^{(1)'}(L)/J^{(2)'}(L)$ ;
- 5 | Analytical Jacobian  $J(s) = J^{(1)}(s) + vJ^{(2)}(s)$ ;
- 6 **else**
- 7 | Analytical Jacobian  $J(s) = J^{(1)}(s)$ ;
- 8 **end**

---

where  $\bar{\vartheta}(\psi) = \text{sgn}(\bar{\vartheta}_2)\sqrt{\bar{\vartheta}_1^2 + \bar{\vartheta}_2^2}$ ,  $\psi_0 := \psi_0(\psi)$  denotes the phase shift and  $\psi_0 = \arctan(\bar{\vartheta}_1/\bar{\vartheta}_2)$ . The equivalence expression of  $\theta_L$  implies that  $\theta_L$  exhibits a periodic sinusoidal-like relation with  $\psi$  and is bounded by  $\bar{\vartheta}$ . These inferences are validated in the following quantitative computations.

The deflection angle  $\theta(s)$  and the analytical Jacobian  $J(s)$  can be obtained by implementing the Algorithm 1. In the shooting method, the second derivative  $\frac{\partial^2\sigma(s, \theta)}{\partial\theta^2}$  used for iteration is estimated through Newton interpolation, leading to efficient convergence with an average number of shooting iterations less than 3 times. Combining (1) and the conclusion in Remark 4, Assumption 2 holds when the position between the magnet and the robot satisfies the resulting inequality:

$$\|\mathbf{p}\| > \frac{1}{\pi} \left( \frac{\mu_0 M_{\mathcal{A}} M A L^2}{EI} \right)^{\frac{1}{3}}. \quad (15)$$

With the material property of MSCR #1 lied in Tab. I, the upon inequality shows  $\|\mathbf{p}\| > 0.1425$  (m). By locating the RME at the top of the MSCR's distal end with height varying from 0.18 m to 0.22 m, a heat map illustrating the values of  $\theta_L$  is demonstrated in Fig. 4.A. The numerical results indicate that as  $\psi$  varies within the range of  $[-\pi, \pi]$ , the sinusoidal-like trend of  $\theta_L$  is well predicted by (14). Similarly, the successfully predicted phase shift contour ( $\theta_L = 0$ ) explains the deflection of MSCR induced by the gradient magnetic field when  $\psi = 0$ . The workspace of the MSCR is determined by the extremums, denoted as  $\theta_L^\vee$  and  $\theta_L^\wedge$ , and it becomes compressed as the RME moves away. The proof of the boundedness and bijection property of  $\theta_L$  is scheduled in Theorem 3. The extreme points  $\psi^\vee$  and  $\psi^\wedge$  are solutions such that  $\frac{\partial\theta_L}{\partial\psi}(\psi) = 0$ . Despite the displacement of the extremums of MSCR at different heights, its periodicity of  $2\pi$  remains unchanged. As depicted in Fig. 4.B, the zero-crossing contour lines of the Jacobian  $J_\psi$  correspond to the extremal trajectories of  $\theta_L$ , and highlighting the singular conditions.

---


$$\begin{aligned} \vartheta(\mathbf{p}_{\mathcal{G}}, \psi) &= \left\{ -\frac{A}{EI} \int_0^L \int_0^\zeta \left[ \left( \frac{\partial\mathbf{R}}{\partial\theta} \mathbf{m} \right)^\top \bar{\mathbf{B}}(\mathbf{p}_{\mathcal{G}}) + \left( \frac{\partial\mathbf{x}}{\partial\theta} \right)^\top \bar{\mathbf{B}}_g(\mathbf{p}_{\mathcal{G}}, \mathbf{R}\mathbf{m}) \right] ds d\zeta \right\} \hat{\mathbf{m}}_{\mathcal{G}}(\psi) \\ &= \bar{\vartheta}(\theta; \mathbf{p}_{\mathcal{G}})\hat{\mathbf{m}}_{\mathcal{G}}(\psi). \end{aligned} \quad (11)$$

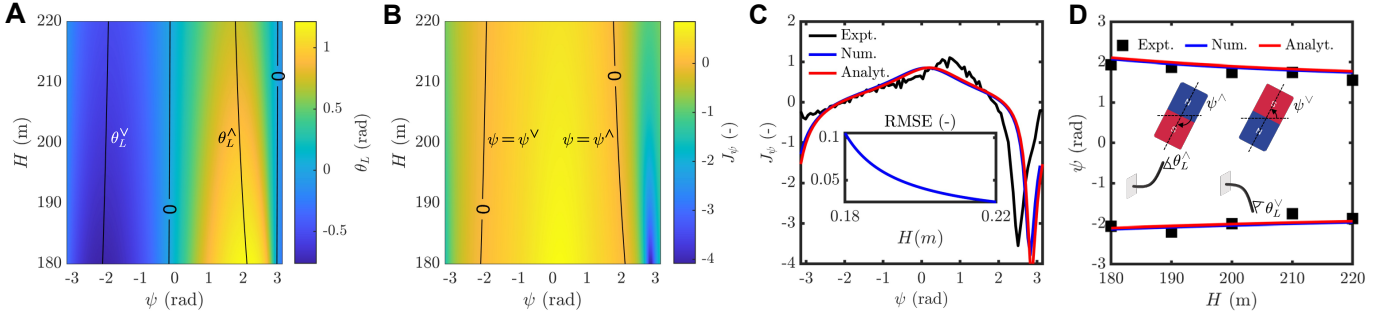


Fig. 4. Heat map of (A) the rotation angle  $\theta_L$  and (B) the Jacobian  $J_\psi$ , with the RME origin located at the distal end of the MSCR, varying in height ( $H$ ) from 0.18 m to 0.22 m. (C) Comparison of the analytical Jacobian ( $\bar{J}_\psi$ ) with the experimental result and numerical Jacobian when the RME positioned at  $H = 0.18\text{m}$  (see Movie S1). (D) Comparison of the experimental, numerical, and analytical Jacobian singularities.

Recall that  $J(s)$  is computed with higher order term  $\nabla^2 \mathbf{b}$  ignored, a comparison between the experimental, numerical, and analytical Jacobian at  $H = 0.18$  (m) is plotted in Fig. 4.C. The results indicate that the analytical Jacobian (denoted as  $\bar{J}_\psi$ ) fits well with the numerical Jacobian (noted as  $\Delta J_\psi$ ), with the root-mean-square-error (RMSE) caused by  $\nabla^2 \mathbf{b}$  terms decreasing as  $H$  increases. Both of them exhibit a good agreement with experimental results and explain the rapid reduction in the deflection angle of MSCR when the magnet crosses the greater singular value  $\psi^\wedge$ . As shown in Movie S1, the magnet briefly loses control over MSCR when crossing  $\psi^\wedge$  and regains control after further rotating. This transient process can be described by the dynamic model proposed in our previous work [25]. Fig. 4.D illustrates the singularities predicted by our model for the magnet at different heights. Our model yields RMSE of 0.1225 (rad) for  $\psi^\wedge$  and 0.1595 (rad) for  $\psi^\vee$ . These accurate estimates are beneficial for precisely determining the control direction and allow the addition of soft constraints to limit the rotation range for RME, thereby preventing loss of control over the MSCR.

### C. Design of the Controller

A closed-loop control scheme is designed for the MSCR to perform quasi-static state transfer and can overcome the model parameter perturbation  $\Delta J_\psi$ . Define the system's state as  $x_1 = \theta_L$ , the input as  $u = \psi$ , and  $x_1(t)$  directly as the output  $y(t)$ . Then, the differential kinematic model is rewritten by

$$\begin{cases} \dot{x}_1(t) = x_2(t) + \bar{J}_\psi u(t) \\ y(t) = x_1(t), \end{cases} \quad (16)$$

where  $x_2(t) \triangleq f(x_1(t), w(t)) + \Delta J_\psi u(t)$  denotes the extended state covering model uncertainties, perturbances, and unknown disturbances. The controllability of this affine nonlinear system is described by the following theorem.

**Theorem 3.** *If Assumptions 1 and 2 are hold, then the distal rotation angle  $\theta_L = \vartheta(\psi)$  exists a value domain  $\Theta \triangleq [\theta_L^\vee, \theta_L^\wedge]$  when  $\psi$  lies in an arbitrarily closed interval  $\Psi \subset \mathbb{R}$ , and the state  $x_1(t) = \theta_L$  of the system (16) is controllable for  $\theta_L \in \Theta$ .*

**Remark 5.** *Notably, the unit vector  $\mathbf{m}_G(\psi) = [\cos(\psi), \sin(\psi), 0]^\top$  exhibits a period length of  $2\pi$ . Thus,*

*when the length of  $\Psi$  exceeds  $2\pi$ ,  $\theta_L$  will encompass a widest domain of  $\Theta$ . Another important result from the above theorem is that  $\theta_L \in \Theta$  forms a monotonic bijective mapping with  $\psi$ , in response to Remark 3.*

The proof of Theorem 3 is provided in Appendix C. As thoroughly elaborated in [26], the extended state observer (ESO) is well-constructed to estimate the total disturbance  $x_2(t)$ . To apply conveniently in practice, a linear ESO (LESO) is employed in the input-affine system (16) as

$$\begin{cases} \dot{\bar{x}}_1(t) = \bar{x}_2(t) + \frac{\beta_1}{\epsilon}(y(t) - \bar{x}_1(t)) + \bar{J}_\psi u(t) \\ \dot{\bar{x}}_2(t) = \frac{\beta_2}{\epsilon^2}(y(t) - \bar{x}_1(t)), \end{cases} \quad (17)$$

where  $\beta_1, \beta_2$  are two pertinent observer gains, and  $\epsilon \geq 0$  is the constant gain. A proportional-derivative (PD) controller is designed as  $u_0(t) = \hat{y}_r(t) + k(\bar{y}_r(t) - \bar{x}_1(t))$ , where  $\bar{y}_r(t)$  and  $\hat{y}_r(t)$  are the tracked and the derivative of the reference signal  $y(t)$  using the tracking differentiator (TD), respectively. A useful linear structure of TD is given by  $\ddot{\bar{y}}_r(t) = -k_1 R^2(\bar{y}_r(t) - y_r(t)) - k_2 R \dot{\bar{y}}_r(t)$ , where  $k_1 > 0, k_2 > 0$  are constants, and  $R > 0$  is the tuning parameter. Note that the stability analysis and the convergence proof of LESO and TD are vividly outlined in [27]. With the extended state  $\bar{x}_2(t)$  uniformly convergence to  $x_2(t)$ , the comprehensive controller that cancels the total disturbance is designed as

$$u(t) = \bar{J}_\psi^{-1}(u_0(t) - \bar{x}_2(t)). \quad (18)$$

It can be readily verified that the upon controller exponentially converges to the reference signal over time. The feedback loop is accomplished by the visual servoing platform, clarified in the following Section IV-B.

## IV. SIMULATIONS AND EXPERIMENTS

This section validates the feasibility of the previously proposed quasi-static control framework. A fast and precise algorithm is developed and deployed on the visual servoing platform to capture the distal rotation angle. The change in control direction introduced by  $J_\psi$  is demonstrated to be necessary in the simulation. The effectiveness of the closed-loop deflection control using PD and quasi-static controller (QSC) is compared. Experimental procedures are provided in the [Supplementary Videos](#).



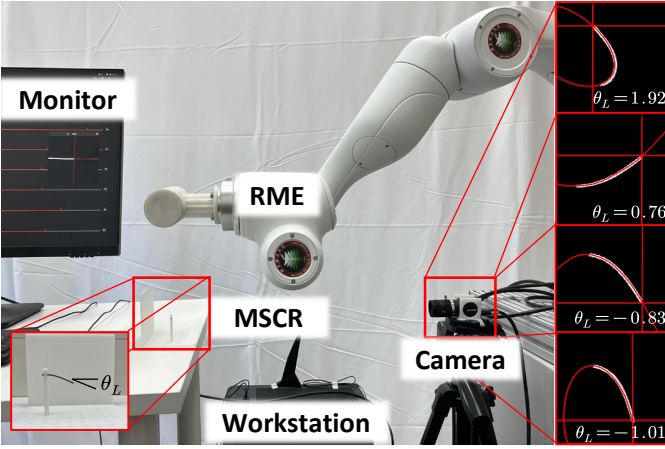


Fig. 5. A photo shot of the experiments with instrumentation. The distal rotation angle of the MSCR is measured by conic section fitting.

TABLE I  
PARAMETERS OF THE MSCRS.

	Parameter (Description)	Value	Unit
MSCR #1	$L$ (length)	24	mm
	$r$ (Radius)	0.54	mm
	$E$ (Young's modulus)	3.0	MPa
	$M$ (Magnitude of magnetization)	8.0	kA/m
MSCR #2	$L$ (length)	30	mm
	$r$ (Radius)	0.65	mm
	$E$ (Young's modulus)	2.8	MPa
	$M$ (Magnitude of magnetization)	9.3	kA/m

### A. System Overview

A photo shot of the experiments with instrumentation is displayed in Fig. 5. The high-performance workstation (Intel<sup>®</sup> Core<sup>™</sup> i5-12490F @3.00GHz processor and 32GB RAM) was utilized for computing control commands and device communication. The system devices are comprised of several components as follows: (1) Magnetically actuated MSCRs were magnetized along the robot's axial direction using a magnetizer (MA-3030, Jiuju Inc., Shenzhen, China). (2) The customized 3D-printed robot fixture platform was employed to clamp the proximal end of the robot and allow flexible configuration of the free end length. (3) Cameras (HKMV-CH050-10VC, Hangzhou Hikrobot Co., Ltd., China) were utilized for visual servoing to achieve closed-loop control of the robot's deflection. (4) The RME was mounted at the end-effector of a robot arm (Diana 7w, AGILE ROBOTS AG, Germany) to ensure reaching desired configurations.

### B. Visual Servoing Platform

The measurement of the MSCR's distal angle  $\theta_L$  is challenging due to the lack of body-load sensors. Currently, visual servoing and emerging magnetic/ultrasonic localization techniques are the mainstream measurement methods [28]–[30]. Image-based visual servoing fits conic sections to the MSCR to capture  $\theta_L$ . This post-processing procedure is outlined in Algorithm 2. The algorithm requires real-time images of the MSCR, typically obtained through deep learning or threshold segmentation, containing continuous pixels from the proximal

to the distal end. The core idea is to obtain the analytical expression of the fitting function at different deformation shapes using LSF, then iteratively compute the pixels or their neighborhood from a starting point to determine if the endpoint is reached. Finally, the derivative at the end-point, representing the tangent slope corresponding to the deflection angle  $\theta_L$ , is calculated.

We utilize the linearity measure  $\ell_e$  to quantify deformation and select the appropriate fitting function. The starting point is based on the image centroid  $P$ , ensuring it remains valid within the robot body. The algorithm results are shown in Fig. 5. For small deflections, a quadratic function is chosen to improve computational speed, with coordinates as the iterative variable. For large deflections, an elliptical equation is used, with the eccentric angle as the iterative variable. By transforming coordinates to the ellipse center, iterative computation is simplified using the standard elliptic parametric equation. The algorithm achieves a frame rate exceeding 75 Hz, capturing the dimensionless distal rotation angle of the MSCR in any configuration without markers on the free end.

---

#### Algorithm 2: Conic section fitting for distal angle

---

**Input:** Real-time binarized image  $P \in \mathbb{R}^{u \times v}$   
**Output:** Conic section fitted distal angle  $\theta_L$

- 1 Compute the centroid pixel coordinates  $(g_x, g_y)$  of  $P$ ;
- 2 Compute the linearity  $\ell_e$  of the MSCR;
- 3 **if**  $\ell_e \leq \text{threshold}$  **then**
  - // small deflection
  - 4 LSF using the quadratic function:  $\bar{v}(\bar{u}) = a^2\bar{u} + b\bar{u} + c$ ;
  - 5 Set the iteration initial point at  $t_x = g_x, t_y = \bar{v}(g_x)$ ;
  - 6 **do**
    - 7  $t_y \leftarrow t_y \pm 2at_x + a^2 \pm b, t_x \leftarrow t_x \pm 1$ ;
    - 8 Compute the pixel at  $([t_x], [t_y])$  (or the sum of its  $3 \times 3$  neighborhood for robustness);
    - 9 **while**  $P([t_x], [t_y]) = 0$ ;
- 10 **else**
  - // large deflection
  - 11 LSF using the elliptical function:  $(\bar{u}, \bar{v})Q(\bar{u}, \bar{v})^T$ ;
  - 12 Coordinates transformation from camera to ellipse  $\{O_\varepsilon\}$ ;
  - 13 Set the iteration initial angle  $\alpha = \arctan(g_y^\varepsilon/g_x^\varepsilon)$ ;
  - 14 **do**
    - 15  $\alpha \leftarrow \alpha \pm 0.1, t_x^\varepsilon = a \cos \alpha, t_y^\varepsilon = b \sin \alpha$ ;
    - // standard elliptic parametric equation
    - 16 Compute the pixel at  $([t_x], [t_y])$  (or the sum of its  $3 \times 3$  neighborhood for robustness);
    - 17 **while**  $P([t_x], [t_y]) = 0$ ;
- 18 **end**
- 19 Compute the slope angle at  $([t_x], [t_y])$  and select the one with the larger absolute value for  $\theta_L$ ;

---

### C. Experimental Results

The measured physical parameters of the MSCR #1 are summarized in Tab. I. The nominal Jacobian  $\bar{J}_{\psi}$  in (18) is obtained by carrying out Algorithm 1. Although our designed control strategy constrains the configuration of the RME, it also enables the three-dimensional deflection of the MSCR to be equivalently represented as a two-dimensional deflection in the  $\varphi$ -plane. Due to the dual operations of attraction and repulsion exerted by the permanent magnet on the MSCR, in

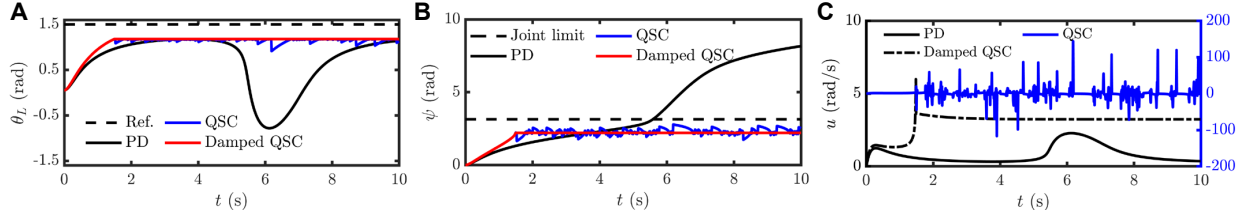


Fig. 6. (A) Comparison of the responses of an unreachable step signal by the PD controller, quasi-static controller (QSC), and damped QSC. (B) Comparison of the rotation angle ( $\psi$ ) of the actuator. Note that the control law generated by the PD controller results in the angle exceeding the joint limit. (C) Comparison of the control law. The chattering in the QSC controller is caused by discontinuities in the Jacobian near singularity.

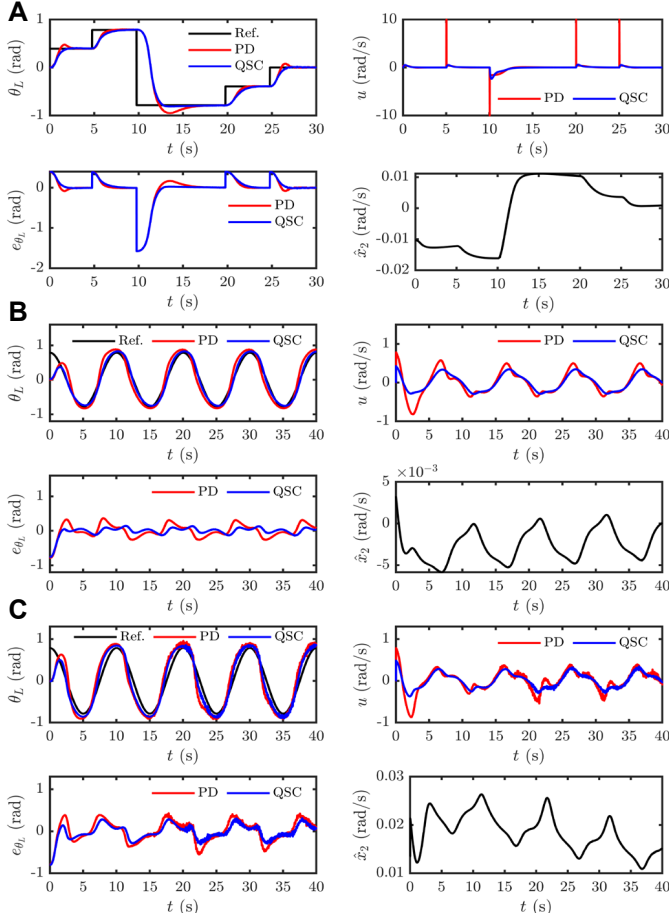


Fig. 7. Comparison of the (A) step-response, (B) cosine-response, and (C) cosine-response with disturbance of MSCR using the QSC and PD controller. The transient processes, control inputs, and estimated total disturbances are plotted in each panel.

situations where the RME is unable to reach certain configurations (e.g., physical collision constraints or joint singularities), tasks can be accomplished by the dual operation from the opposite side. For the sake of simplicity in measuring the distal angle, we select the  $\hat{x}_G\text{-}\hat{y}_G$  plane to validate the performance of the quasi-static controller. During the experimental process, the origin of the RME remains fixed above the distal end of the MSCR at the height of 18.0 cm, and the initial rotation angle is set to zero. However, because of the existing gradient magnetic field, the MSCR undergoes slight deflections as shown in Fig. 4.A, which gradually diminishes as the RME moves further away. The initial value of  $\theta_L$  is then set to zero,

and as demonstrated in Movies S2-S4, the rotation angle of the RME stabilizes close to  $\varphi_0$ . The parameters of the LESO are designed as  $\beta_1 = 1$ ,  $\beta_2 = 0.01$ , and  $\epsilon = 0.01$ , while the parameters of TD are set as  $R = 10$ ,  $k_1 = 0.1$ , and  $k_2 = 1$ . As for the PD controller,  $k = 1.02$ .

We first validate the necessity of introducing the change in control direction brought about by  $J_\psi$  through simulations. Previous analysis has indicated that the system is bounded under any initial conditions. In practical applications, it is difficult to avoid setting reference signals that extend beyond the system's state range  $\Theta$ . Therefore, when the actuator is near the extreme points  $\psi^\wedge$  or  $\psi^\vee$ , the sign of  $J_\psi$  may change and potentially cause singular issues in the system. A straightforward solution inspired from [31] is to introduce a damping form for the structural change of  $J_\psi$  as follows:

$$J_\psi = \begin{cases} J_\psi, & |J_\psi| \geq \lambda \\ \text{sgn}(J_\psi)\lambda, & |J_\psi| < \lambda, \end{cases} \quad (19)$$

where  $\lambda$  is a small positive constant. We refer to the QSC with this structure introduced as the damped QSC. This approach directly prevents the system from velocity singularities when  $J_\psi$  becomes singular.

In Fig. 6.A, the system's response to an unreachable step signal using PD, QSC, and damped QSC controllers is shown. The PD controller, lacking the correct control direction, produces residual errors that persist after extremum points, forcing continuous actuator operation. As seen in Fig. 6.B, this incorrect control direction causes the actuator to reach the joint limit around 5.8 seconds, posing safety risks. In contrast, QSC, with the correct control direction, stabilizes the system near output limits, keeping the actuator within safe joint limits. However, Jacobian singularities cause high-frequency chattering, leading to the spiky output seen in Fig. 6.C. Damped QSC mitigates this chattering, stabilizing the system near extremums with a smooth control law and safe actuator operation. In summary, the control direction introduced by  $J_\psi$  protects system components and enhances performance.

Within the workspace of the MSCR, a comparison is conducted between the step responses of the MSCR using the PD controller and QSC approach (see Movie S2). As shown in Fig. 7.A, under the same parameter conditions, the QSC approach significantly eliminates overshoot while maintaining a fast response. This improvement can be attributed to the reliable nominal controller gains provided by  $\bar{J}_\psi$ , regulating the controller parameters, and the incorporation of the ESO for



estimating unmodeled dynamics  $\bar{x}_2$ . The performance error plot illustrates the trade-off between speed and overshoot introduced by the PD controller, whereas QSC's overshoot-free tracking reduces potential collisions with vascular walls. Moreover, the control input  $u$  generated by the QSC approach, optimized using TD, smooths out the pulsating waves produced by the PD controller, avoiding potential hardware damage and ensuring refined control operations.

Further comparison is made between the cosine responses of the MSCR using two different controllers (see Movie S3). As shown in Fig. 7.(b), the QSC approach achieves fast and overshoot-free tracking of the cosine signal, exhibiting greatly improved control performance at peaks compared to the PD controller under the same parameter conditions. The estimated perturbations  $\bar{x}_2$  demonstrate periodic behavior and gradual convergence, consistent with the previous theoretical analysis. Additionally, as shown in the performance error plots, the QSC approach effectively reduces the energy consumption of the controller, with a reported average steady-state error of 0.062, outperforming the PD controller's value of 0.1364. To validate the robustness of the controller in the presence of external disturbances (for clinical surgeries, consider vascular vibrations and hemodynamic impacts caused by the patient's cardiac pacing), a separate set of experimental tests was conducted in a wind disturbance environment starting from 15 seconds (see Movie S4). The results demonstrated that the control performance of the PD controller significantly deteriorated, with a steady-state error of 0.2005. In contrast, the QSC approach maintained a high tracking accuracy, and the impact of high-frequency noise in the system output on the state estimate of the ESO is minor, with a reported steady-state error of 0.1299.

Overall, the proposed quasi-static control framework effectively enhances the transient performance and steady-state error of the PD controller. However, the controller may encounter some challenges in higher-frequency signals (period  $\leq 5$  s), possibly due to the lag in the velocity control.

## V. EXTENSION TO POSITIONAL CONTROL

Some critical scenarios place control demands on the tip position of the MSCR, which usually involves computing the Jacobian matrix between the task-space and the actuation-space of the distal end position. The Jacobian we solved for the rotation angle can be conveniently applied to compute this matrix. As we mentioned previously, when the proximal end of the MSCR is fixed, the workspace of the tip position is limited and approximates a hemispherical surface. To expand the workspace, we add a linearly movable base to the MSCR, and its displacement is represented by  $\nu$ . The workspace of the movable MSCR is shaped like a cylinder in Fig. 8.A, and its radius is determined by the maximum displacement of the tip position  $\|\mathbf{x}_L\|_{\max}$ . Fig. 8.B compares the displacement of the MSCR's distal end between simulation and experiment when the magnet is at different rotation angles and heights. The simulation and experimental results show good consistency, indicating that the model can reasonably estimate the Jacobian matrix and maximum displacement (marked in black circles).

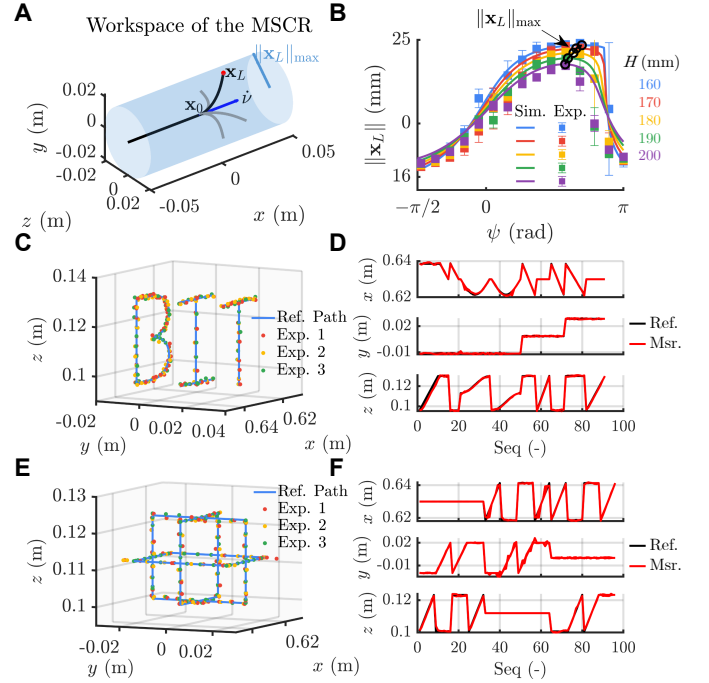


Fig. 8. (A) Illustration of the workspace of the MSCR. (B) Comparison of displacement of the MSCR's distal end between simulation and experiment when the magnet is at different rotation angles and heights. (C and E) Path-following control of two paths with each of three experimental results. (D and F) Comparison of reference with average measured distal end position for each spatial coordinate.

Let  $\mathbf{x}_0(\nu)$  be the proximal end of the movable MSCR, and take the roll angle  $\varphi = 0$  as an example, the body coordinates satisfy the following kinematic equations:

$$\mathbf{x}(s) = \mathbf{x}_0 + \left( \int_0^s \cos \theta(\eta) d\eta \hat{\mathbf{x}}_G + \int_0^s \sin \theta(\eta) d\eta \hat{\mathbf{y}}_G \right). \quad (20)$$

The differential kinematics is then derived as

$$\dot{\mathbf{x}}_L = \left[ \frac{\partial \mathbf{x}_L}{\partial \nu}, \frac{\partial \mathbf{x}_L}{\partial \psi} \right] \begin{bmatrix} \dot{\nu} \\ \dot{\psi} \end{bmatrix} \triangleq \mathbf{B} \mathbf{u}, \quad (21)$$

where the components of the Jacobian matrix ( $\mathbf{B}$ ) is given by

$$\frac{\partial \mathbf{x}_L}{\partial \psi} = - \int_0^L \sin \theta \frac{\partial \theta}{\partial \psi}(\eta) d\eta \hat{\mathbf{x}}_G + \int_0^L \cos \theta \frac{\partial \theta}{\partial \psi}(\eta) d\eta \hat{\mathbf{y}}_G,$$

and  $\frac{\partial \mathbf{x}_L}{\partial \nu} = [1, 0, 0]^\top$ . The corresponding closed-loop controller can be designed as

$$\mathbf{u} = \dot{\mathbf{x}}_L^r + k_x \mathbf{B}^\dagger (\mathbf{x}_L^r - \mathbf{x}_L), \quad (22)$$

in which  $k_x$  is a positive constant and  $(\cdot)^\dagger$  denotes in the Moore-Penrose pseudo-inverse.

In the predicted MSCR workspace, two path-following control (PFC) tasks are designed to examine the controller's performance. The material properties of MSCR #2 in Tab. I is employed, and the controller gain is set to  $k_x = 0.5$ . The distal end is marked, and a stereo camera captures the position. Each path was sampled with more than 90 points. A path point is considered reached when the relative rate of change in positional error falls below 1%. Three sets of

positional experiments were conducted for each path. The results indicate that the positional RMSE for the path in Fig. 8.C was  $0.965 \pm 0.156$  (mm), while for Fig. 8.E, the positional error was  $0.972 \pm 0.396$  (mm). The comparisons between the reference and the average measured distal end position for each spatial coordinate are shown in Fig. 8.D and Fig. 8.F, respectively. Overall, the positional error accounts for only 3.22% and 3.24% of the MSCR length, which demonstrates the effectiveness of our designed controller in achieving high-precision control over the MSCR's distal end.

## VI. CONCLUSIONS

In this study, we achieved closed-loop deflection control of MSCRs by utilizing a single rotatable permanent magnet as the end-effector of the robot arm. The proposed kinematic model effectively characterizes the quasi-static states of MSCR in different configurations in a non-uniform magnetic field. The existence and uniqueness of Jacobian are supported theoretically, and the estimation of singularities is highly consistent with experimental results. The designed damping structure for Jacobian effectively mitigates the control law oscillations when crossing singularities. Experimental results demonstrated that the proposed QSC framework outperformed the PD controller in terms of steady-state accuracy and transient performance during trajectory tracking. Extensions are made for the path-following control of the distal end position, and the positional error is only sub-millimeter. This framework holds promise for precise intravascular navigation of MSCRs in the future. However, some unresolved issues remain, such as the inapplicability of camera-based visual platforms for in vivo surgeries. Future work will further explore the closed-loop control of MSCR combined with angiographic image guidance.

## APPENDIX

### A. Proof of Theorem 1

*Proof.* It can be readily observed that the function  $\sigma(s, \theta)$  is continuous on  $\mathcal{R} : 0 \leq s \leq L, \theta^2 + \theta'^2 \leq \infty$ . We show the derivative of  $\sigma(s, \theta)$  with respect to  $\theta$ , written in the shorthand form as

$$\begin{aligned} \frac{EI}{A} \frac{\partial \sigma(s, \theta)}{\partial \theta} &= -\frac{\partial^2}{\partial \theta^2} (\mathbf{Rm} \cdot \mathbf{b}) \\ &= \mathbf{Rm} \cdot \left( \mathbf{b} + \nabla \mathbf{b} \mathbf{x} - \nabla^2 \mathbf{b} \frac{\partial \mathbf{x}}{\partial \theta} \frac{\partial \mathbf{x}}{\partial \theta} \right) \\ &\quad + 2\mathbf{e}_z \cdot \left( \mathbf{Rm} \times \nabla \mathbf{b} \frac{\partial \mathbf{x}}{\partial \theta} \right), \end{aligned} \quad (23)$$

in which  $\nabla^2 \mathbf{b}$  is a 3-order tensor. Since  $\forall s \in [0, L], \|\mathbf{p}_A - \mathbf{x}(s)\| > 0$ , it follows that both the magnitude of  $\mathbf{b}$  and of its higher-order gradient tensors are bounded. Using  $\|\cdot\|$  for all tensors, we obtain that  $\frac{\partial \sigma(s, \theta)}{\partial \theta}$  is uniformly bounded in  $\mathcal{R}$  by

$$\begin{aligned} &\left| \frac{\partial \sigma(s, \theta)}{\partial \theta} \right| \\ &< \frac{MA}{EI} \left[ B + \|\nabla \mathbf{b}\| \left( \|\mathbf{x}\| + 2 \left\| \frac{\partial \mathbf{x}}{\partial \theta} \right\| \right) + \|\nabla^2 \mathbf{b}\| \left\| \frac{\partial \mathbf{x}}{\partial \theta} \right\|^2 \right] \\ &\leq \frac{MA}{EI} (B + 3\|\nabla \mathbf{b}\|L + \|\nabla^2 \mathbf{b}\|L^2) \triangleq K \end{aligned} \quad (24)$$

where we used the Cauchy-Schwarz inequality:

$$\begin{aligned} \left\| \frac{\partial \mathbf{x}}{\partial \theta} \right\| &= \sqrt{\left( -\int_0^s \sin \theta(\eta) d\eta \right)^2 + \left( \int_0^s \cos \theta(\eta) d\eta \right)^2} \\ &\leq \sqrt{s \int_0^s \sin^2 \theta(\eta) + \cos^2 \theta(\eta) d\eta} \\ &= s \leq L. \end{aligned} \quad (25)$$

Hence, a Lipschitz constant can be taken as  $K$ , which depends only on the physical parameters of the MSCR and magnet. Given the fact that  $\frac{\partial \sigma(s, \theta)}{\partial \theta'} = 0$ , both  $\frac{\partial \sigma(s, \theta)}{\partial \theta}$  and  $\frac{\partial \sigma(s, \theta)}{\partial \theta'}$  satisfy the Lipschitz condition. This conclusion, according to the existence theorems for solutions of BVP ([22]), completes the proof.  $\square$

### B. Proof of Theorem 2

*Proof.* Define two unique functions  $J^{(1)}(s)$  and  $J^{(2)}(s)$  on  $[0, L]$  as solutions of the respective initial value problems: (a)  $LJ^{(1)} = \frac{\partial \sigma}{\partial \psi}$ ;  $J^{(1)}(0) = 0, J^{(1)'}(0) = 0$  and (b)  $LJ^{(2)} = 0$ ;  $J^{(2)}(0) = 0, J^{(2)'}(0) = 1$ . The function  $J(s)$  defined by  $J(s) = J(s; v) \triangleq J^{(1)}(s) + vJ^{(2)}(s), 0 \leq s \leq L$  satisfies  $J(0) = 0$  and will thus be a solution of problem (10) if  $v$  is chosen such that  $\phi(v) \triangleq J'(L; v) = 0$ . The equation is linear in  $v$  and has the single root  $v = -J^{(1)'}(L)/J^{(2)'}(L)$ , provided that  $J^{(2)'}(L) \neq 0$ .

In the proof of Theorem 1, we conclude that  $\frac{\partial \sigma}{\partial \psi}$  is bounded by  $K$  when Assumption 1 holds. Consequently, invoking the comparison principle, we can assert that  $\underline{\mathcal{J}}'(s) < J^{(2)'}(s) < \overline{\mathcal{J}}'(s)$  for  $s \in [0, L]$ , where  $\underline{\mathcal{J}}(s)$  and  $\overline{\mathcal{J}}(s)$  are solutions to the following differential equations:  $\frac{d^2 \underline{\mathcal{J}}(s)}{ds^2} = -K\underline{\mathcal{J}}(s)$  and  $\frac{d^2 \overline{\mathcal{J}}(s)}{ds^2} = K\overline{\mathcal{J}}(s)$ , subject to the same initial values as  $J^{(2)}(s)$ . Analytical solutions for  $\underline{\mathcal{J}}'(s)$  and  $\overline{\mathcal{J}}'(s)$  are found in  $\underline{\mathcal{J}}'(s) = \cos(\sqrt{K}s)$  and  $\overline{\mathcal{J}}'(s) = \cosh(\sqrt{K}s)$ , respectively. Since the Lipschitz constant  $K \in \mathcal{K}$ , it is guaranteed that  $\overline{\mathcal{J}}'(L) = \cosh(\sqrt{K}L) > 0$  and  $\underline{\mathcal{J}}'(L) = \cos(\sqrt{K}L) > 0$ , which leads to  $J^{(2)'}(L) > 0$ . Hence,  $LJ^{(2)}$  has a nontrivial solution, and the SL-BVP (10) has a unique solution  $J(s)$ .  $\square$

### C. Proof of Theorem 3

*Proof.* We first prove the existence of  $\Theta$ . The parameter  $\psi$  can be separated from functions  $\sigma(s, \theta; \psi)$  and  $\frac{\partial \sigma(s, \theta; \psi)}{\partial \theta}$  as  $\sigma(s, \theta; \psi) = \varsigma(s, \theta) \hat{\mathbf{m}}_{\mathcal{G}}(\psi)$  and  $\frac{\partial \sigma(s, \theta; \psi)}{\partial \theta} = \frac{\partial \varsigma(s, \theta)}{\partial \theta} \hat{\mathbf{m}}_{\mathcal{G}}(\psi)$ , where  $\hat{\mathbf{m}}_{\mathcal{G}}(\psi) : \mathbb{R} \rightarrow \mathbb{R}^3$  is a smooth unit vector function. Thus,  $\sigma(s, \theta; \psi)$  and  $\frac{\partial \sigma(s, \theta; \psi)}{\partial \theta}$  are continuously differentiable in  $\psi$ . Note that  $J_{\psi} = J(s; \psi)|_{s=L}$ , where  $J(s; \psi) = J^{(1)}(s; \psi) + vJ^{(2)}(s; \psi)$  is the linear composition of solutions to two initial-value problems. Based on the continuity theorem of the solutions with respect to parameters, the Jacobian  $J_{\psi}$  is continuous over any closed interval  $\Psi$ . Consequently,  $\vartheta(\psi)$  exhibits the same continuity property as  $J_{\psi} = \frac{d\vartheta(\psi)}{d\psi}$ . Then, as a function continuous on a closed interval is bounded there, it is found a value domain of  $\theta_L$  by  $\Theta \triangleq [\theta_L^{\vee}, \theta_L^{\wedge}]$ .

We then prove the controllability. Given an initial state  $\theta_L(t_0) \in \Theta$ , the corresponding rotation angle  $\psi(t_0) = \vartheta^{-1}(\theta_L(t_0)) \in \Psi$ . Then, for any final state  $\theta_L(t_f) \in \Theta$ ,

there always exists a corresponding rotation angle  $\psi(t_f) = \vartheta^{-1}(\theta_L(t_f))$  by the intermediate value theorem. Hence, the admissible control input can be taken as  $u = \frac{\psi(t_f) - \psi(t_0)}{t_f - t_0}$ , and thus the controllability is proved. Throughout the proof, Assumption 1 guarantees the existence of  $\theta(s)$ , and Assumption 2 guarantees the existence and uniqueness of  $J(s)$ .  $\square$

## ACKNOWLEDGMENT

The author would like to thank Siyi Wei and Zhanxin Geng for their invaluable assistance and contributions to this work. Additionally, the author extends gratitude to all the reviewers for their significant contributions to improving this paper.

## REFERENCES

- [1] J. F. Schenck, "Safety of strong, static magnetic fields," *Journal of Magnetic Resonance Imaging*, vol. 12, no. 1, pp. 2–19, 2000.
- [2] F. Kong, Y. Zhu, C. Yang, H. Jin, J. Zhao, and H. Cai, "Integrated locomotion and deformation of a magnetic soft robot: Modeling, control, and experiments," *IEEE Transactions on Industrial Electronics*, vol. 68, no. 6, pp. 5078–5087, Jun. 2021.
- [3] W. Lee, J. Nam, J. Kim, E. Jung, N. Kim, and G. Jang, "Steering, tunneling, and stent delivery of a multifunctional magnetic catheter robot to treat occlusive vascular disease," *IEEE Transactions on Industrial Electronics*, vol. 68, no. 1, pp. 391–400, Jan. 2021.
- [4] C. Fischer, Q. Boehler, and B. J. Nelson, "Using magnetic fields to navigate and simultaneously localize catheters in endoluminal environments," *IEEE Robotics and Automation Letters*, vol. 7, no. 3, pp. 7217–7223, Jul. 2022.
- [5] J. Hwang, J.-y. Kim, and H. Choi, "A review of magnetic actuation systems and magnetically actuated guidewire-and catheter-based micro-robots for vascular interventions," *Intelligent Service Robotics*, vol. 13, pp. 1–14, 2020.
- [6] F. Carpi and C. Pappone, "Stereotaxis niobe® magnetic navigation system for endocardial catheter ablation and gastrointestinal capsule endoscopy," *Expert review of medical devices*, vol. 6, no. 5, pp. 487–498, 2009.
- [7] "Stereotaxis earns fda clearance and announces u.s. launch of genesis robotic magnetic navigation system," <https://www.cathlabdigest.com/content/stereotaxis-earns-fda-clearance-and-announces-us-launch-genesis-robotic-magnetic-navigation-system>, Fri, 03/06/2020 - 09:40.
- [8] A. W. Mahoney and J. J. Abbott, "Five-degree-of-freedom manipulation of an untethered magnetic device in fluid using a single permanent magnet with application in stomach capsule endoscopy," *The International Journal of Robotics Research*, vol. 35, no. 1-3, pp. 129–147, Jan. 2016.
- [9] Y. Kim, E. Genevriere, P. Harker, J. Choe, M. Balicki, R. W. Regenhardt, J. E. Vranic, A. A. Dmytriw, A. B. Patel, and X. Zhao, "Telerobotic neurovascular interventions with magnetic manipulation," *Science Robotics*, vol. 7, no. 65, p. eabg9907, Apr. 2022.
- [10] Y. Kim, G. A. Parada, S. Liu, and X. Zhao, "Ferromagnetic soft continuum robots," *Science Robotics*, vol. 4, no. 33, p. eaax7329, 2019.
- [11] T. Haidegger, "Autonomy for surgical robots: Concepts and paradigms," *IEEE Transactions on Medical Robotics and Bionics*, vol. 1, no. 2, pp. 65–76, May 2019.
- [12] J. Edelmann, A. J. Petruska, and B. J. Nelson, "Magnetic control of continuum devices," *The International Journal of Robotics Research*, vol. 36, no. 1, pp. 68–85, Jan. 2017.
- [13] T. L. Thomas, J. Sikorski, G. K. Ananthasuresh, V. K. Venkiteswaran, and S. Misra, "Design, sensing, and control of a magnetic compliant continuum manipulator," *IEEE Transactions on Medical Robotics and Bionics*, vol. 4, no. 4, pp. 910–921, Nov. 2022.
- [14] G. Pittiglio, A. L. Orekhov, T. da Veiga, S. Calò, J. H. Chandler, N. Simaan, and P. Valdastri, "Closed loop static control of multi-magnet soft continuum robots," *IEEE Robotics and Automation Letters*, vol. 8, no. 7, pp. 3980–3987, Jul. 2023.
- [15] K. Abolfathi, J. A. Rosales-Medina, H. Khaksar, J. H. Chandler, K. D. McDonald-Maier, K. Ashkan, P. Valdastri, and A. K. Hoshjar, "Independent and hybrid magnetic manipulation for full body controlled soft continuum robots," *IEEE Robotics and Automation Letters*, vol. 8, no. 7, pp. 4235–4242, Jul. 2023.

- [16] T. Liu, R. Jackson, D. Franson, N. L. Poirot, R. K. Criss, N. Seiberlich, M. A. Griswold, and M. C. Çavuşoğlu, "Iterative jacobian-based inverse kinematics and open-loop control of an mri-guided magnetically actuated steerable catheter system," *IEEE/ASME Transactions on Mechatronics*, vol. 22, no. 4, pp. 1765–1776, Aug. 2017.
- [17] D. Lin, W. Chen, K. He, N. Jiao, Z. Wang, and L. Liu, "Position and orientation control of multisection magnetic soft microcatheters," *IEEE/ASME Transactions on Mechatronics*, vol. 28, no. 2, pp. 907–918, Apr. 2023.
- [18] S. Wei, J. Zhang, Z. Wu, and D. Chen, "Magnetic robot for endovascular intervention: Performance evaluation," *IEEE Transactions on Industrial Electronics*, vol. 71, no. 10, pp. 12592–12600, 2024.
- [19] A. J. Petruska and J. J. Abbott, "Optimal permanent-magnet geometries for dipole field approximation," *IEEE Transactions on Magnetics*, vol. 49, no. 2, pp. 811–819, Feb. 2013.
- [20] J. J. Abbott, E. Diller, and A. J. Petruska, "Magnetic methods in robotics," *Annu. Rev. Control Robot. Auton. Syst.*, vol. 3, no. 1, pp. 57–90, May 2020.
- [21] L. Wang, Y. Kim, C. F. Guo, and X. Zhao, "Hard-magnetic elastica," *Journal of the Mechanics and Physics of Solids*, vol. 142, p. 104045, Sep. 2020.
- [22] H. B. Keller, *Numerical methods for two-point boundary-value problems*. Courier Dover Publications, 2018.
- [23] L. Lu, J. Sim, and R. R. Zhao, "Mechanics of hard-magnetic soft materials: A review," *Mechanics of Materials*, p. 104874, 2023.
- [24] S. N. Ha, "A nonlinear shooting method for two-point boundary value problems," *Computers & Mathematics with Applications*, vol. 42, no. 10-11, pp. 1411–1420, 2001.
- [25] Z. Wu, J. Zhang, S. Wei, and D. Chen, "Kirchhoff rod-based three-dimensional dynamical model and real-time simulation for medical-magnetic guidewires," *Computer Methods and Programs in Biomedicine*, p. 107646, 2023.
- [26] J. Han, "From pid to active disturbance rejection control," *IEEE Trans. Ind. Electron.*, vol. 56, no. 3, pp. 900–906, Mar. 2009.
- [27] B.-Z. Guo and Z.-L. Zhao, *Active Disturbance Rejection Control for Nonlinear Systems: An Introduction*. Singapore: John Wiley & Sons Singapore Pte. Ltd, Oct. 2016.
- [28] Z. Yang, L. Yang, M. Zhang, C. Zhang, S. C. H. Yu, and L. Zhang, "Ultrasound-guided catheterization using a driller-tipped guidewire with combined magnetic navigation and drilling motion," *IEEE/ASME Transactions on Mechatronics*, vol. 27, no. 5, pp. 2829–2840, Oct. 2022.
- [29] M. Zhang, L. Yang, C. Zhang, Z. Yang, and L. Zhang, "A 5-d large-workspace magnetic localization and actuation system based on an eye-in-hand magnetic sensor array and mobile coils," *IEEE Trans. Instrum. Meas.*, vol. 72, pp. 1–11, 2023.
- [30] J. Sikorski, A. Denasi, G. Bucchi, S. Scheggi, and S. Misra, "Vision-based 3-d control of magnetically actuated catheter using bigmag—an array of mobile electromagnetic coils," *IEEE/ASME Transactions on Mechatronics*, vol. 24, no. 2, pp. 505–516, Apr. 2019.
- [31] S. R. Buss and J.-S. Kim, "Selectively damped least squares for inverse kinematics," *Journal of Graphics tools*, vol. 10, no. 3, pp. 37–49, 2005.



**Zhiwei Wu** was born in Fujian, China, in 2000. He received a B.E. degree from the College of Information Science and Technology, Beijing University of Chemical Technology, Beijing. He is currently working towards a Ph.D. degree in the Department of Automation at the Beijing Institute of Technology, Beijing. His research interests include surgical robotic systems and the control of magnetic soft continuum robots.



**Jinhui Zhang** received the Ph.D. degree in control science and engineering from the Beijing Institute of Technology, Beijing, China, in 2011. He was an Associate Professor with the Beijing University of Chemical Technology, Beijing, from 2011 to 2016. He joined the Beijing Institute of Technology in 2016, where he is currently a Professor. His research interests include networked control systems and composite disturbance rejection control.